1	Recent state transition of the Arctic Ocean's Beaufort Gyre
2	
3	Peigen Lin <sup>1,2</sup> , Robert S. Pickart <sup>2</sup> ,
4	Harry Heorton <sup>3</sup> , Michel Tsamados <sup>3</sup> ,
5	Motoyo Itoh <sup>4</sup> , Takashi Kikuchi <sup>4</sup>
6	
7	1. School of Oceanography, Shanghai Jiao Tong University, China
8	2. Woods Hole Oceanographic Institution, USA
9	3. Department of Earth Sciences, Centre for Polar Observation and Modelling, University
10	College London, UK
11	4. Institute of Arctic Climate and Environment Research, Japan Agency for Marine-Earth
12	Science and Technology, Yokosuka, Japan
13	
14	
15	
16	
17	
18	
19	
20	
21	
22	
23	Revised for Nature Geoscience
24	March 2023
25	
26	Corresponding Author: Peigen Lin (plinwhoi@gmail.com)
27	

#### 28 Abstract

The anti-cyclonic Beaufort Gyre is the dominant circulation of the Canada Basin and the largest freshwater reservoir in the Arctic Ocean. During the first part of the 2000s the gyre intensified, expanded, and accumulated freshwater. Using an extensive hydrographic dataset from 2003-2019, together with updated satellite dynamic ocean topography data, we find that over the past decade the Beaufort Gyre has transitioned to a quasi-stable state in which the increase in sea surface height of the gyre has slowed and the freshwater content has plateaued. In addition, the cold halocline layer, which isolates the warm/salty Atlantic water at depth, has thinned significantly due to less input of cold and salty water stemming from the Pacific Ocean and the Chukchi Sea shelf, together with greater entrainment of lighter water from the eastern Beaufort Sea. This recent transition of the Beaufort Gyre is associated with a southeastward shift in its location as a result of variation in the regional wind forcing. Our results imply that continued thinning of the cold halocline layer could modulate the present stable state, allowing for a freshwater release. This in turn could freshen the subpolar North Atlantic, impacting the Atlantic Meridional Overturning Circulation.

56 The Beaufort Gyre is the largest freshwater reservoir in the Arctic Ocean<sup>1-3</sup>, driven by the 57 anti-cyclonic winds in the Canada Basin<sup>4</sup>. Since 2000 the gyre has strengthened and its freshwater content has increased by 40% relative to the 1970's climatology<sup>5</sup>. Associated with the 58 59 accumulating freshwater, the gyre has expanded northwestward<sup>6,7</sup>, and its layer of cold Pacificorigin water has widened laterally and thickened vertically<sup>8</sup>. There are many potential impacts of 60 61 the changing Beaufort Gyre on the hydrographic structure, physical processes, and ecosystem of the Arctic, both local and remote. As such, it is of high interest to better understand the factors 62 63 associated with such changes – including the underlying causes.

The gyre strength generally coincides with the intensity of the surface forcing<sup>3,9</sup>, which is a 64 combination of the wind-ocean stress (or simply wind stress) and the ice-ocean stress<sup>10,11</sup>. As the 65 gyre spins up, the acceleration of the geostrophic circulation reduces the ice-ocean stress which 66 in turn weakens the forcing and acts to stabilize the gyre<sup>12</sup>. Another negative feedback with 67 respect to forcing is that the growing freshwater content and enhanced halocline tilting generate 68 69 more eddies via baroclinic instability, which in turn dampen the gyre and flatten the halocline<sup>13</sup>. 70 Both modeling and satellite sea surface height measurements have suggested that the Beaufort 71 Gyre stabilized from 2008 to 2014<sup>9,14</sup>. However, it is unknown if this represented an overall 72 change in the state of the gyre. Furthermore, the underlying reasons for any such change have 73 not been addressed observationally.

74 A major source of the interannual variation in freshwater content of the Beaufort Gyre is the Pacific-origin water entering through Bering Strait<sup>5</sup>. A substantial portion of this water is 75 subsequently fluxed off the Chukchi shelf through Barrow Canyon<sup>15</sup>, and ultimately enters the 76 gyre<sup>16-18</sup>. River runoff, particularly from the Mackenzie River, is believed to contribute nearly 77 equally to the interannual variation<sup>5,19</sup>. Our study investigates the long-term trends of the 78 79 Beaufort Gyre and reveals that it has transitioned to a quasi-stable state over the last decade. 80 We use an extensive updated collection of historical hydrographic data and satellite dynamic 81 ocean topography data to characterize this state and provide insights into the reasons for the 82 change. We quantify the evolution of the gyre in terms of its sea surface height and freshwater content, and explore the connection to the cold halocline layer. As the gyre has evolved to its 83 84 recent state the halocline has thinned considerably, the causes of which are addressed.

85

#### 86 Long-term trend of the Beaufort Gyre

87 The state of Beaufort Gyre (BG) is reflected by the dynamic ocean topography (DOT) 88 averaged over the BG region (Fig. 1a, see Extended Data Fig. 1 for the DOT climatology). The 89 newly-updated DOT data presented here extend the timeseries to 2019. The spatially averaged 90 DOT of the BG generally increased from 2003-2019 (Fig. 1b), but there are notable variations 91 around this trend. We divide the record into two time periods: 2003-2011 and 2012-2019. The 92 break point was objectively chosen by computing the trends corresponding to a 4-year running 93 window over the DOT timeseries. It revealed that the trend reaches a minimum (close to zero) in 94 the period 2010-2013 (the results are not sensitive to a one-year shift in the break point). In the 95 first period there was a strong increase in the average DOT throughout the BG region, with a 96 maximum trend in the northwest Canada Basin where the gyre expanded to (Fig. 2a; consistent with a previous result<sup>7</sup>). Since that time the BG has continued to strengthen, but at a considerably 97 98 slower rate (with a short weakening from 2011-2013, Fig. 1b). Unlike the earlier period, the 99 increase in DOT occurred predominantly in the southeast part of the Canada Basin (Fig. 2c). 100 Meanwhile, a decreasing trend is found west of the Chukchi Plateau. These changes indicate that, 101 over the last decade, the BG has contracted and shifted to the southeast part of the basin (see 102 also Extended Data Fig. 2). We note that, while a large part of this shift occurred 2019, the trend 103 is still significant when excluding that year.

104 To illustrate how the freshwater content (FWC) has varied in relation to the changes in the 105 strength of the BG, we calculated the annual mean FWC using the historical hydrographic data 106 (FWC<sub>1</sub> in the Methods, Fig. 1c). To compare with previous studies, we also computed the 107 freshwater volume as the FWC multiplied by the area of the BG region. The FWC was 108 approximately 14.6 m in 2003 and increased to over 20 m in 2011, equivalent to an increase in freshwater volume from 16,000 km<sup>3</sup> to over 22,000 km<sup>3</sup> (consistent with previous observational 109 estimates<sup>1</sup>). This corresponds to a trend of 940 km<sup>3</sup> yr<sup>-1</sup>. However, the situation changed 110 111 dramatically in the second period when the freshwater volume underwent fluctuations between 112 22,000 and 24,000 km<sup>3</sup>. During this time there was no statistically significant trend. We also 113 constructed a timeseries of FWC using the DOT data together with estimates of the ocean mass

from GRACE (FWC<sub>2</sub> in the Methods), as well as the associated freshwater volume. These two FWC estimates are in phase with each other (r=0.92, p<0.01) and have comparable trends, indicating that the BG has entered a quasi-stable regime whereby the increase of the DOT has slowed and the FWC has plateaued.

118

#### 119 Thinning of Cold Halocline Layer

120 We now investigate the response of the water column in the BG region during the second period. Beneath the surface layer, the halocline acts to inhibit upward mixing of the warm deep 121 122 Atlantic water that otherwise could result in substantial ice melt<sup>1</sup>. In the western Arctic the warm halocline, which originates from the Pacific summer water<sup>4,18</sup>, sits atop the cold halocline which 123 124 is ventilated by cold and salty winter water formed/modified locally on the shelves of the Chukchi and Beaufort Seas via brine rejection<sup>20,21</sup>. The warm halocline layer corresponds to a salinity (S) 125 126 range of 28 to 32.6, while the cold halocline layer (CHL) spans the range 32.6 to 33.9. These ranges 127 were identified using mean vertical profiles within the BG (see Methods).

128 We computed trends in the volume of water within salinity classes spanning the warm and 129 cold haloclines in the BG region for the two periods considered above (Fig. 3). In the first period 130 the trends are positive for *S* > 30, particularly in the CHL. The thickening halocline coincides with 131 the increasing DOT in the early period (Fig. 1b). By contrast, the trends are significantly negative in the CHL in the later period, peaking at -600 km<sup>3</sup> yr<sup>-1</sup> for waters with  $S \sim 33$ , while the trends 132 remain relatively close to zero at shallower depths. This suggests that the thinning of the CHL 133 134 results in the thinning of the entire halocline. One might then ask, what is the impact of changes 135 in the thickness of the CHL on the layer thickness of the entire freshwater reservoir lying above 136 the Atlantic water?

To address this, we constructed thickness anomaly timeseries, relative to the value in 2003, for (1) the CHL layer; (2) the layer from the surface to the top of the CHL (comprised of the warm halocline and the surface layer); and (3) the sum of these two; i.e., the full layer above the underlying Atlantic water (Fig. 1d). Associated with the changes of DOT and FWC, the full layer thickened markedly by 5.8 m yr<sup>-1</sup> in the early period, due mostly to thickening of the layer above the CHL, although the CHL did undergo a net expansion during this period. By contrast, since 2012 the CHL has been thinning at a rate of -1.5 m yr<sup>-1</sup>, offsetting the expansion of the upper layer and
causing a plateau in total thickness. The steric effect of the plateaued layer plays a role in the
slower increase in DOT<sup>22</sup>. This trend in the thickness of the CHL has not been spatially uniform,
however (Fig. 2e): while thinning has occurred over a large portion of the BG region, particularly
west of the Chukchi Plateau, the layer has thickened in the southeast portion of the Canada Basin.
This agrees well with the spatial trends of DOT and FWC during the second period (Fig. 2c,d).

149 It has been argued that the relocation and expansion of the BG during the early period was 150 caused primarily by the strengthening atmospheric Beaufort High and its enhanced negative wind 151 stress curl<sup>7,9</sup>. To further investigate the role of atmospheric forcing during the second period, we 152 constructed a map of the trend of wind stress curl from 2012-2019 (Fig. 2f). A negative trend of 153 wind stress curl is evident in the southeast part of the Canada basin where the DOT, FWC and 154 CHL thickness have increased. This makes sense dynamically in that enhanced negative wind 155 stress curl leads to stronger Ekman pumping, which in turn causes these changes. At the same 156 time, the negative trends of DOT, FWC and CHL thickness to the west of the Chukchi Plateau is 157 likely associated with the positive trend of wind stress curl in this region. This highlights the 158 interconnectedness of the different attributes of the Beaufort gyre and their relationship to the 159 atmospheric Beaufort High.

160

#### 161 **Causes of the thinning CHL**

Pacific-origin winter water is the main source water that ventilates the CHL in the western 162 Arctic Ocean<sup>8,18</sup>. Concomitant with the increased Bering Strait inflow, the Pacific water has 163 164 become markedly warmer and fresher. These changes suggest that the Pacific winter water 165 which previously ventilated the CHL in the 1990s likely now more readily affects the shallower 166 layer in the basin<sup>23</sup>. This is in line with our results showing the recent thinning of the CHL and the 167 thickening of the layer immediately above (Fig. 3). However, as the Pacific winter water transits 168 across the Chukchi shelf, its salinity can be increased via brine rejection during ice formation in polynyas and leads <sup>20,24,25</sup>. Hence, it is unclear how these offsetting effects have been playing out. 169 170 Since a significant portion of Pacific-origin water flows into the basin through Barrow Canyon, we

now use mooring data at the canyon mouth to further elucidate the source water that eventuallyimpacts the CHL in the BG region.

173 Fig. 3 shows the trends of the volume of water fluxed off the shelf through Barrow Canyon 174 in each salinity class through the water column. One sees that in both periods the trends of the 175 Barrow Canyon outflow are in line with the volume trends in the basin computed above; in 176 particular, positive trends in the CHL from 2003-2011, peaking above the CHL layer, and negative 177 trends from 2012-2019, with the maximum near a salinity of 33 within the CHL. Note, however, 178 that the trends of the Barrow Canyon outflow water that supplies the CHL are smaller than the 179 ones in the basin (although they are not significantly different), and the discrepancy is greater in 180 the later years. These results thus indicate two important aspects regarding ventilation in the 181 basin: the Barrow Canyon outflow water cannot solely explain the total trend of the CHL in the 182 BG, and the contribution from the canyon is reduced in the later years.

183 Cold and salty winter water is also regularly formed along the eastern Beaufort Sea shelf and fluxed offshore by downwelling<sup>21</sup>. It has been previously emphasized that the contribution of 184 185 freshwater from the eastern Beaufort Sea is comparable to the Pacific-origin water<sup>5</sup>. It is thus 186 reasonable to consider the winter water formed in the eastern Beaufort Sea as the other 187 important source water of the CHL in the BG, and how this source water might respond to the 188 spatial change of the BG. It is worth noting that the Barrow Canyon outflow can feed the eastern Beaufort Sea via the eastward-flowing Beaufort shelfbreak jet<sup>26</sup>. However, the jet is centered 189 190 near the 150 m isobath and is bottom-intensified in the mean, particularly in the cold months<sup>27</sup>, 191 and thus it has a minor impact on the winter water on the shelf.

192 To investigate the impact of the eastern source of winter water in the different BG regimes, 193 we conducted Lagrangian particle experiments based on the annual mean velocity field averaged 194 over the CHL from the GLORYS12 ocean reanalysis product (the GLORYS12 velocities show good 195 agreement with mooring data in the western Arctic, Extended Data Fig. 3). The first experiment 196 was done for the extreme year of 2011, at the end of the early period when the DOT core of the 197 BG was located at its northwestern-most location during this period (Fig. 4a, note that the BG 198 reached the extreme northwestern position in 2013). Particles denoted by blue and red colors 199 were released along the 100 m isobath in the Chukchi Sea/western Beaufort Sea (CS/WBS) and

200 eastern Beaufort Sea (EBS), respectively (Fig. 4b). After one year, most of the CS/WBS particles 201 progressed into the BG region near the Chukchi Plateau. The majority of these parcels emanated 202 from the eastern side of Barrow Canyon and subsequently turned to the west, consistent with previous observational and modeling studies<sup>28,29</sup>. By contrast, most of the EBS particles stayed 203 204 very close to the location where they were released. To quantify this, we computed the 205 percentage of the CS/WBS and EBS particles that resided for more than half the year in the BG 206 region (within the purple polygon in Fig. 1a). This revealed that 90% of the CS/WBS particles did 207 so, compared to only 15% for the EBS particles.

208 A second experiment was then conducted for the extreme year of 2019, at the end of the 209 later period when the DOT core of the BG had shifted to the southeastern-most location during 210 this period (Fig. 4a). In this case, 84% of the CS/WBS particles progressed into the BG region near 211 the Chukchi Plateau, slightly less than the first experiment. However, the percentage of EBS 212 particles reaching this region increased dramatically to 73%. This suggests that the contribution 213 of the EBS water to the CHL is dynamically linked to the BG state: when the gyre shifts to the 214 southeast, the CHL is more likely to be significantly ventilated by winter water emanating from 215 the eastern Beaufort Sea shelf.

216 The question remains as to the role of the EBS water in the thinning of the CHL. To address 217 this, we used the historical hydrographic data and computed the fractional occurrence of the 218 water in each of the salinity classes of Fig. 3 on the EBS shelf (128-147°W and shoreward of 100-219 m isobath) and on the CS/WBS shelf (147-165°W, shoreward of 100-m isobath and extending 220 southward to 70.5°N or to the coast). This revealed that, for the warm halocline layer, the 221 fractional occurrence was similar for the two regions, while for the CHL the fractional occurrence 222 was larger on the CS/WBS shelf. This, together with fact that the area of the CS/WBS shelf is 223 greater than that of the EBS, implies that the potential source volume of water that can ventilate 224 cold halocline layer is larger on the CS/WBS shelf. Assuming that the CHL source water in the EBS originates from the inner shelf<sup>21</sup>, it gives a volume supply of ~400 km<sup>3</sup>, substantially less than the 225 226 annual mean volume of the water fluxed via Barrow Canyon, ~2400 km<sup>3</sup>, estimated from the moorings. Hence, during the second period when there is enhanced influence from the EBS (Fig. 227 228 4c), the amount of available shelf water in the salinity class of the CHL is less, implying that the

CHL would thin. We conclude then that both the reduced Barrow Canyon outflow and the
southeast shift in the BG location led to the reverse in trend of the CHL thickness from the early
to the late period.

232

#### 233 Discussion

Our results have demonstrated that, during the last decade, the BG has transitioned to a quasi-stable state, shifting towards the southeast Canada Basin where the negative wind stress curl has intensified, together with a dampened rate of increase of sea surface height, stabilization of freshwater content, and thinning of the CHL. The recent decrease in the amount of Pacificorigin winter water exiting Barrow Canyon explains some of the CHL thinning, while the enhanced influence from the eastern Beaufort Sea – due to the southeastward shift of the BG – likely contributes as well.

241 Previous work has demonstrated that the local wind patterns modulating the BG are related to the large-scale Arctic Oscillation (AO)<sup>4</sup>. On interannual timescales, positive AO states are 242 243 associated with a contracted BG situated in the southeast Canada Basin, while negative AO states 244 correspond to an expanded BG. A similar relationship holds on decadal timescales, with a 245 northwestward expansion and movement during 2003-2011 when the AO index was mostly 246 negative, and southeastward shift during 2012-2019 when the AO was mainly in the positive state 247 (Extended Data Fig. 4). We emphasize, however, that the recent state of the BG documented here does not represent a return to the initial condition of 2003 when the gyre was weak and 248 249 located partially in the southeastern basin. Instead, under the strengthened wind stress curl, the 250 gyre has continuously intensified even though it has contracted (Fig. 4a), and it has maintained 251 its excess freshwater storage. That said, with a steric effect of the continued thinning of the CHL 252 due to a decrease in the source winter water, the DOT of the gyre may be further stabilized or 253 perhaps begin to drop, disrupting the freshwater accumulation in the gyre. A recent study has 254 shown that the FWC in the gyre slightly dropped in 2020-2021<sup>30</sup>. If these conditions continue 255 going forward, it could cause a pronounced salinity anomaly to progress through the Canadian 256 Arctic Archipelago into the Labrador Sea and/or through Fram Strait into the Nordic Seas<sup>31-33</sup>. It 257 is argued that half of the freshwater from Arctic is diverted into the north Atlantic interior,

providing the major source of freshening in the Atlantic Meridional Overturning Circulation, while
the other half joins the estuarine circulation along the boundary<sup>34</sup>. As was the case with the Great
Salinity Anomaly<sup>35</sup>, as well as with the recent major freshening event from 2012-2016<sup>36</sup>, this will
likely impede wintertime convection, which could impact the Atlantic Meridional Overturning
Circulation<sup>37</sup>, a key component of global climate<sup>38</sup>.

263

#### 264 Acknowledgements

Funding for the study was provided by National Science Foundation grant OPP-1733564 and National Oceanic and Atmospheric Administration grant NA19OAR4320074 (P.L., R.S.P.); Shanghai Pujiang Program 22PJ1406400 and Shanghai Frontiers Science Center of Polar Science (P.L.); European Space Agency Project (ESA/AO/1-9132/17/NL/MP and ESA/AO/1-10061/19/I-EF) and Natural Environment Research Council (NE/T000546/1 and NE/X004643/1) (M.T.); Arctic Challenge for Sustainability projects (ArCS and ArCSII) of the Ministry of Education, Culture, Sports, Science and Technology (M.I., T.K.).

272

## 273 Author contributions

P.L. led the data analysis and resulting interpretation, with assistance from all co-authors. P.L.
and R.S.P. wrote the manuscript with input from all co-authors. H.H. and M.T. produced the
updated dynamic ocean topography data from 2011-2019. M.I. and T.K. provided the long-term
data from the mooring array at the mouth of Barrow Canyon.

278

## 279 Competing Interests

- 280 The authors declare no competing interests.
- 281

### 282 Figure captions

Fig. 1 | Long-term trends of the Beaufort Gyre: 2003-2011 versus 2012-2019. a, Geographic map of the Arctic Ocean with an enlarged view of the study region (black box). The schematic Beaufort Gyre (BG) is marked by the yellow circle. The Beaufort Gyre region is delimited by 130°-180°W, 81°N and 300 m isobath (thick purple line), over which area averages (± standard errors) are 287 computed, shown in b-d. The bathymetry from IBCAO v3 is colored, with the isobaths of 40, 70, 288 150, 250, 500 m in grey, and 100 and 300 m highlighted in black. **b**, The annual mean BG dynamic 289 ocean topography (DOT, m); c, The annual mean BG freshwater content (m) and volume ( $\times 10^4$ 290 km<sup>3</sup>) estimated using the historical hydrographic data (FWC<sub>1</sub>, magenta) and using the DOT + 291 GRACE data (FWC<sub>2</sub>, green); d, The annual mean BG thickness anomalies (m) relative to 2003 of 292 the layer from the surface to the top of the cold halocline (yellow), the cold halocline layer 293 beneath this (purple), and the sum of the two layers (orange). The standard error is the standard 294 deviation divided by square root of the degrees of freedom, where the degrees of freedom for 295 each year (ranging from 12 to 71) are computed using an integral time scale of 3 days for the 296 hydrographic data and one month for the monthly satellite data. The dashed lines are the linear 297 trends in the early and late periods, and the black lines in b and c denote the linear trends of DOT 298 and FWC<sub>1</sub> over the full study period, respectively. The trends were computed using the timeseries 299 of annual-mean variables.

300

301 Fig. 2 | Spatial distribution of the trends in the Beaufort Gyre region. a,c, Trends of dynamic 302 ocean topography in the early period (2003-2011) and in the late period (2012-2019); b,d, trends 303 of the freshwater content in the early period and in the late period; **e**,**f**, trends of the thickness 304 of the cold halocline layer and the wind stress curl in the late period. The dots represent the areas 305 with statistically significant trends (subsampled every 5 points for the DOT data, every 4 points 306 for the FWC and CHL thickness, and every 5 points in longitude for the wind stress curl). The line connecting the two centers of the trends (76.78 $^{\circ}$  N, 179.6 $^{\circ}$  W and 72.87 $^{\circ}$  N, 139.37 $^{\circ}$  W) in c 307 308 is used to construct the Hovmöller plot in Fig. 4a.

309

Fig. 3 | Linear trends of volume within salinity classes in relation to the source water. Trends of volume in the Beaufort Gyre region (BG, curves) and in the main source water at the mouth of Barrow Canyon (BC, filled circles), in the early period (2003-2011, blue) and the late period (2012-2019, red). The 95% confidence intervals of the trends are denoted by the dashed lines and horizontal bars. The shaded region is the cold halocline layer.

315

Fig. 4 | Inferred contributions to the cold halocline layer (CHL) in the Beaufort Gyre region. a, 316 317 Hovmöller diagram of dynamic ocean topography (DOT, m) along the line in Fig. 2c from 2003 to 318 2019 (upper panel), with the dots denoting the maximum DOT projected onto the line in each 319 year, and the horizontal solid line separating the two time periods. The associated bathymetry is 320 shown (bottom panel), where the east and west edges of the Chukchi Plateau are denoted by the 321 vertical dashed lines. **b**, The Lagrangian particle experiment in 2011. The 0.45 m DOT contour representing the location of the Beaufort Gyre is shown (black curve). The particles are released 322 along the 100 m isobath in the Chukchi Sea/western Beaufort Sea (CS/WBS, blue stars) and in the 323 324 eastern Beaufort Sea (EBS, red stars). The trajectories of the particles after one year are colored 325 light blue for the CS/WBS and light red for the EBS. c, same as b except for the experiment in 326 2019.

327

## 328 References

- Proshutinsky, A., Krishfield, R. & Timmermans, M. L. Introduction to special collection on
   Arctic Ocean modeling and observational synthesis (FAMOS) 2: Beaufort Gyre
   phenomenon. J. Geophys. Res. Oceans 125, e2019JC015400 (2020).
- Proshutinsky, A. *et al.* Beaufort Gyre freshwater reservoir: State and variability from
   observations. *J. Geophys. Res. Oceans* **114** (2009).
- 334 3 Timmermans, M. L. & Marshall, J. Understanding Arctic Ocean circulation: A review of 335 ocean dynamics in a changing climate. *J. Geophys. Res. Oceans* **125**, e2018JC014378 336 (2020).
- 337 4 Steele, M. *et al.* Circulation of summer Pacific halocline water in the Arctic Ocean. *J.*338 *Geophys. Res. Oceans* **109** (2004).
- 339 5 Proshutinsky, A. *et al.* Analysis of the Beaufort Gyre freshwater content in 2003–2018. *J.*340 *Geophys. Res. Oceans* 124, 9658-9689 (2019).
- Armitage, T. W. *et al.* Arctic Ocean surface geostrophic circulation 2003–2014. *The Cryosphere* 11, 1767-1780 (2017).
- Giles, K. A., Laxon, S. W., Ridout, A. L., Wingham, D. J. & Bacon, S. Western Arctic Ocean
  freshwater storage increased by wind-driven spin-up of the Beaufort Gyre. *Nature Geoscience* 5, 194-197 (2012).
- 3468Zhong, W., Steele, M., Zhang, J. & Cole, S. T. Circulation of Pacific winter water in the347Western Arctic Ocean. J. Geophys. Res. Oceans 124, 863-881 (2019).
- Regan, H. C., Lique, C. & Armitage, T. W. The Beaufort Gyre extent, shape, and location
  between 2003 and 2014 from satellite observations. *J. Geophys. Res. Oceans* 124, 844862 (2019).
- 35110Tsamados, M. *et al.* Impact of variable atmospheric and oceanic form drag on352simulations of Arctic sea ice. J. Phys. Oceanogr. 44, 1329-1353 (2014).

- Yang, J. The Seasonal Variability of the Arctic Ocean Ekman Transport and Its Role in the Mixed Layer Heat and Salt Fluxes. J. Clim. 19, 5366-5387 (2006).
  Meneghello, G., Marshall, J., Timmermans, M.-L. & Scott, J. Observations of seasonal upwelling and downwelling in the Beaufort Sea mediated by sea ice. J. Phys. Oceanogr.
  48, 795-805 (2018).
- Manucharyan, G. E. & Spall, M. A. Wind-driven freshwater buildup and release in the
  Beaufort Gyre constrained by mesoscale eddies. *Geophys. Res. Lett.* 43, 273-282,
  doi:10.1002/2015gl065957 (2016).
- 36114Zhang, J. et al. The Beaufort Gyre intensification and stabilization: A model -362observation synthesis. J. Geophys. Res. Oceans 121, 7933-7952 (2016).
- 36315Itoh, M., Nishino, S., Kawaguchi, Y. & Kikuchi, T. Barrow Canyon volume, heat, and364freshwater fluxes revealed by long term mooring observations between 2000 and3652008. J. Geophys. Res. Oceans 118, 4363-4379 (2013).
- Lin, P., Pickart, R. S., Moore, G., Spall, M. A. & Hu, J. Characteristics and dynamics of
  wind-driven upwelling in the Alaskan Beaufort Sea based on six years of mooring data. *Deep Sea Res. II* 162, 79-92 (2019).
- Lin, P., Pickart, R. S., Våge, K. & Li, J. Fate of warm Pacific water in the Arctic basin. *Geophys. Res. Lett.* 48, e2021GL094693 (2021).
- Timmermans, M. L., Marshall, J., Proshutinsky, A. & Scott, J. Seasonally derived
  components of the Canada Basin halocline. *Geophys. Res. Lett.* 44, 5008-5015 (2017).
- Krishfield, R. A. *et al.* Deterioration of perennial sea ice in the Beaufort Gyre from 2003
  to 2012 and its impact on the oceanic freshwater cycle. *J. Geophys. Res. Oceans* 119,
  1271-1305 (2014).
- 37620Itoh, M. *et al.* Interannual variability of Pacific Winter Water inflow through Barrow377Canyon from 2000 to 2006. J. Oceanogr. 68, 575-592 (2012).
- 37821Lin, P. *et al.* On the nature of wind-forced upwelling and downwelling in Mackenzie379Canyon, Beaufort Sea. *Prog. Oceanogr.* **198**, 102674 (2021).
- 38022Stammer, D. Steric and wind induced changes in TOPEX/POSEIDON large scale sea381surface topography observations. J. Geophys. Res. Oceans 102, 20987-21009 (1997).
- Woodgate, R. A. & Peralta Ferriz, C. Warming and Freshening of the Pacific Inflow to
   the Arctic from 1990 2019 implying dramatic shoaling in Pacific Winter Water
- ventilation of the Arctic water column. *Geophys. Res. Lett.* **48**, e2021GL092528 (2021).
- Pacini, A. *et al.* Characteristics and transformation of Pacific winter water on the Chukchi
  Sea shelf in late spring. *J. Geophys. Res. Oceans* **124**, 7153-7177 (2019).
- Pickart, R. S. *et al.* Circulation of winter water on the Chukchi shelf in early Summer. *Deep Sea Res. II* 130, 56-75 (2016).
- Lin, P. *et al.* Circulation in the vicinity of Mackenzie Canyon from a year-long mooring
  array. *Prog. Oceanogr.* **187**, 102396 (2020).
- Nikolopoulos, A. *et al.* The western Arctic boundary current at 152°W: Structure,
- 392 variability, and transport. *Deep Sea Research II* **56**, 1164-1181,
- 393 doi:10.1016/j.dsr2.2008.10.014 (2009).

394	28	Leng, H., Spall, M. A., Pickart, R. S., Lin, P. & Bai, X. Origin and Fate of the Chukchi Slope
395		Current Using a Numerical Model and In - situ Data. J. Geophys. Res. Oceans,
396		e2021JC017291 (2021).
397	29	Li, M. et al. Circulation of the Chukchi Sea shelfbreak and slope from moored timeseries.
398		<i>Prog. Oceanogr.</i> <b>172</b> , 14-33, doi:10.1016/j.pocean.2019.01.002 (2019).
399	30	Timmermans, ML. & Toole, J. M. The Arctic Ocean's Beaufort Gyre. Ann. Rev. Mar. Sci.
400		<b>15</b> , 223-248 (2023).
401	31	Karpouzoglou, T., de Steur, L., Smedsrud, L. H. & Sumata, H. Observed changes in the
402		Arctic freshwater outflow in Fram Strait. J. Geophys. Res. Oceans 127, e2021JC018122
403		(2022).
404	32	Rudels, B. Volume and freshwater transports through the Canadian Arctic Archipelago-
405		Baffin Bay system. J. Geophys. Res. Oceans <b>116</b> (2011).
406	33	Zhang, J. <i>et al.</i> Labrador Sea freshening linked to Beaufort Gyre freshwater release.
407		Nature communications 12, 1-8 (2021).
408	34	Le Bras, I. et al. How much Arctic fresh water participates in the subpolar overturning
409		circulation? J. Phys. Oceanogr. 51, 955-973 (2021).
410	35	Gelderloos, R., Straneo, F. & Katsman, C. A. Mechanisms behind the temporary
411		shutdown of deep convection in the Labrador Sea: Lessons from the Great Salinity
412		Anomaly years 1968–71. <i>J. Clim.</i> <b>25</b> , 6743-6755 (2012).
413	36	Holliday, N. P. et al. Ocean circulation causes the largest freshening event for 120 years
414		in eastern subpolar North Atlantic. Nature communications <b>11</b> , 585 (2020).
415	37	Lazier, J. R. Oceanographic conditions at ocean weather ship Bravo, 1964–1974.
416		Atmosphere-ocean <b>18</b> , 227-238 (1980).
417	38	Haine, T. W. et al. Arctic freshwater export: Status, mechanisms, and prospects. Global
418		and Planetary Change <b>125</b> , 13-35 (2015).

419

## 420 Methods

421 Historical hydrographic data. We have assembled an extensive historical hydrographic dataset 422 that consists of temperature and salinity profiles measured by ships, expendable probes, ice-423 tethered profilers, and gliders, from four sources: (a) the World Ocean Database 2018 (WOD18), 424 obtained from the National Centers for Environmental Information, spanning from 1849-2020 in 425 the Arctic Ocean; (b) the Unified Database for Arctic and Subarctic Hydrography (UDASH), which 426 is a composite dataset of salinity and temperature profiles in the domain north of 65°N covering 427 1980-2015<sup>39</sup>; (c) a collection of hydrographic data from the Chukchi Sea from various international sources, spanning 1922-2019<sup>40</sup>; and (d) additional hydrographic profiles in the 428 429 Beaufort Gyre from the Arctic Data Center and the Beaufort Gyre Exploration Project<sup>1</sup>. We removed duplicate profiles. In this study we focus on the data from 2003 to 2019 (Extended DataFig. 5).

While the datasets above have been previously scrutinized, further quality control and error checking were applied as described in Lin et al.<sup>17</sup>. To construct maps of the variables we gridded the data using a Laplacian-spline interpolation scheme<sup>41</sup> with a grid spacing of 1° in longitude and 0.25° in latitude. Further gridding was done for salinity bins, spanning the range 28-34 with an interval of 0.2, and trends were computed using this gridded product.

437

438 Dynamic ocean topography. We employ the monthly altimetry-derived dynamic ocean 439 topography (DOT, sea surface height referenced to the geoid) product from 2003-2014, with a 440 resolution of 0.75° x 0.25° <sup>42</sup>. Following the previous methodology, we extended the time series 441 using the original processing algorithm for the full CryoSat2 time series and up to 88°N. The 442 algorithm is described briefly here, with the reader referred to Armitage et al.<sup>42</sup> for the full 443 technical description. Satellite open ocean surface elevations were obtained from the Low-444 Resolution mode (LRM) and Synthetic Aperture Rader (SAR) ocean modes, and from leads (cracks 445 in the sea ice cover) from SAR Ice and SAR Interferometric modes (SARIn). The UCL13 Mean Sea 446 Surface product was used to calculate the Sea Level Anomaly (SLA) for all four modes. A monthly 447 mean SLA offset of LRM to SAR ocean, SAR ocean to SAR lead, SAR lead to SARIn lead, from 448 coincident measurements on a 100-km resolution grid was calculated to remove mode bias 449 compared to the LRM mode SLA. Following this, the GOCO03s geoid was used to calculate the 450 DOT, removing the bias from the sea level anomaly calculation. The individual DOT and SLA 451 measurements were collected onto the 0.75° x 0.25° grid with outliers above and below the 10th 452 percentiles removed. A smoothed DOT using a 100 km Gaussian kernel was created with the 453 gradient taken to give geostrophic surface currents. Following the repeat usage of the Armitage 454 et al. algorithm<sup>42</sup>, differences between the original and updated datasets over the period 2011-455 2014, are less than 1%.

456

457 **Moorings**. Japan Agency for Marine-Earth Science and Technology (JAMSTEC) has maintained 458 three moorings across the mouth of Barrow Canyon (Extended Data Fig. 5) since 2001, except for

459 the four years of Jun 2004 – Sep 2005, Sep 2008 – Aug 2010, and Oct 2013 – Aug 2014<sup>15</sup>. The 460 central mooring is situated in the center of Barrow Canyon (BCC), and the other two moorings 461 are located on the eastern and western flanks (BCE and BCW, respectively). All three moorings were equipped with MicroCATs for measuring hourly temperature and salinity, and Acoustic 462 463 Doppler Current Profilers (ADCPs) or point current meters for measuring velocities every 0.25-2 464 hours. The ADCP velocity profiles have bin sizes between 4-8 m. The accuracies of the sensors are 0.001 °C for temperature, 0.01 for salinity, and 0.01 m s<sup>-1</sup> for velocity<sup>20</sup>. The temperature, 465 466 salinity and velocity are gridded along the section across the mouth of Barrow Canyon, with a 467 grid size of 2 km in the horizontal and 2 m in the vertical. Due to the lack of data in the upper 50 468 m, the gridded vertical sections only cover the portion of the water column deeper than salinity = 31. The volume of water fluxed across the section in each year is calculated by the mean velocity, 469 470 cross sectional area, and time. In this study, we use the data from 2003 to 2019, consistent with the DOT data. The climatological mean DOT for this period is shown in Extended Data Fig. 1. 471

472

473 **Reanalysis data**. We compute wind stress curl using the hourly wind data from the ERA5 474 reanalysis, provided by the European Center for Medium-Range Weather Forecasts (ECMWF)<sup>43</sup>. 475 The ERA5 is the fifth generation ECMWF reanalysis product with a grid spacing of  $0.25^{\circ} \times 0.25^{\circ}$ . 476 It has been widely used in previous high-latitude studies<sup>17</sup>.

We make use of the velocity data in the cold halocline layer from the global eddy-resolving physical ocean and sea ice reanalysis (GLORYS12)<sup>44</sup>, obtained from the Copernicus Marine and Environment Monitoring Service (CMEMS). GLORYS12 is a NEMO-based reanalysis that assimilates satellite observations and historical hydrographic profiles. It has a horizontal resolution of 1/12°, and 50 vertical levels with increased resolution in the upper layer (1-30 m interval in the upper 200 m).

We compared the GLORYS12 velocities with mooring data at various locations in the western Arctic. Extended Data Fig. 3 shows the two examples of the comparison: a) in the vicinity of the Bering Strait<sup>45</sup> (r=0.76, p<0.01); b) at shelfbreak in the western Beaufort Sea<sup>16</sup> (r=0.54, p<0.01). The good agreements motivated us to use the reanalysis velocity field to carry out the Lagrangian particle experiments in the study.

489 GRACE. We use the monthly equivalent water thickness from the GRACE/GRACE-FO Mascon solutions (release-06, version 2) from the Center for Space Research (CSR)<sup>46</sup> in combination with 490 491 the DOT data to estimate the freshwater content (see below). There are 31 months of gaps in the 492 two-decade record due to the satellite's regular battery management. To fill each of the gaps, 493 we apply a 5-month weighting window centered at the month in question<sup>42</sup>. This technique was 494 not applicable for 2017-2018 when there were successive gap months. In this case, we filled each 495 gap with the mean of the same month from the year before and after. The GRACE data have a 496 spatial resolution of 0.25°, and were interpolated onto the same grid as the DOT data.

497

498 Vertical structure of the water column. The different vertical layers considered in the study are 499 depicted in Extended Data Fig. 6 using mean hydrographic profiles from the Beaufort Gyre. The 500 base of surface layer is defined as the depth at which the potential density difference exceeds 0.125 kg m<sup>-3</sup> from the mean density in upper 10 m<sup>47</sup>. Below that, the halocline in the Canada 501 502 Basin consists of the warm halocline layer and the cold halocline layer<sup>18</sup>. The warm halocline layer 503 is between the base of surface layer and the first minimum in buoyancy frequency below the 504 maximum value. Below this is the cold halocline, the base of which is determined using the ratio 505  $R = \alpha \Delta T / \beta \Delta S$ , where  $\alpha$  is the thermal expansion coefficient and  $\beta$  is the haline contraction coefficient<sup>48</sup>. In particular, the depth where R=0.05, at which point the vertical density gradient 506 507 is mainly due to the salinity gradient, as taken to be the base of cold halocline. The Atlantic water 508 layer resides below this.

509

Freshwater content. The freshwater content is calculated as  $FWC_1 = \int_h^0 \frac{(Sr-S(z))}{Sr} dz$ , applied using the historical hydrographic data over the Beaufort Gyre region<sup>2</sup>. The reference salinity *Sr* is 34.8 at the corresponding depth *h*, and *S*(*z*) is the depth-dependent salinity. For each year, we interpolated the FWC<sub>1</sub> within the Beaufort Gyre region using the Laplacian-Spline interpolation<sup>41</sup>, with a resolution of 1° in the longitude and 0.25° in the latitude, and then computed the mean value.

488

516 We also use the DOT and GRACE data to estimate the annual freshwater content following the methodology used in previous studies<sup>5,7,42</sup>,  $FWC_2 = \frac{S_r - S_1}{S_r} \Delta h$ . In particular, as a 517 518 simplification, the water column in the Beaufort Gyre can be considered as two homogeneous layers: a lighter layer with density  $\rho_1$ =1022 kg m<sup>-3</sup> atop a denser layer with density  $\rho_2$ =1028 kg 519 m<sup>-3</sup>. Variations in the freshwater content alter the thickness of the upper layer  $\Delta h =$ 520  $\eta\left(1+\frac{\rho_1}{\rho_2-\rho_1}\right)-\frac{\Delta m}{\rho_2-\rho_1}$ , which is reflected by the DOT ( $\eta$ ) and ocean mass ( $\Delta m$ ). The  $\Delta m$  is 521 estimated using the GRACE equivalent water thickness multiplied by the water density. The mean 522 523 freshwater volume over the Beaufort Gyre region is computed as the spatial-mean freshwater 524 content (FWC<sub>1</sub> or FWC<sub>2</sub>) multiplied by the area of the Beaufort Gyre region.

525

526 Lagrangian particle experiments. The two Lagrangian particle experiments carried out in the 527 study make use of the GLORYES12 reanalysis velocity data. We first computed the annual mean 528 velocity in the cold halocline layer for the two extreme years of 2011 and 2019. For each 529 experiment, we then released 150 particles along the 100 m isobath within the cold halocline 530 layer in the Chukchi Sea/western Beaufort Sea (CS/WBS) and eastern Beaufort Sea (EBS), and 531 computed the trajectories given the annual mean velocity field. At each time step, the velocity at 532 the nearest grid point to where the particle is located is used to compute the distance traveled 533 over one day. This procedure is iterated for a year.

534

#### 535 Data availability

- 536 The historical hydrographic data are obtained from the following sources.
- 537 (1) the Unified Database for Arctic and Subarctic Hydrography (UDASH,
- 538 https://doi.pangaea.de/10.1594/PANGAEA.872931).
- 539 (2) World Ocean Database 2018 (WOD18, https://www.ncei.noaa.gov/products/world-ocean-540 database).
- 541 (3) Arctic Data Center (https://arcticdata.io/catalog/data)
- 542 (4) Beaufort Gyre Exploration Project (https://www2.whoi.edu/site/beaufortgyre/data/data-
- 543 overview/)

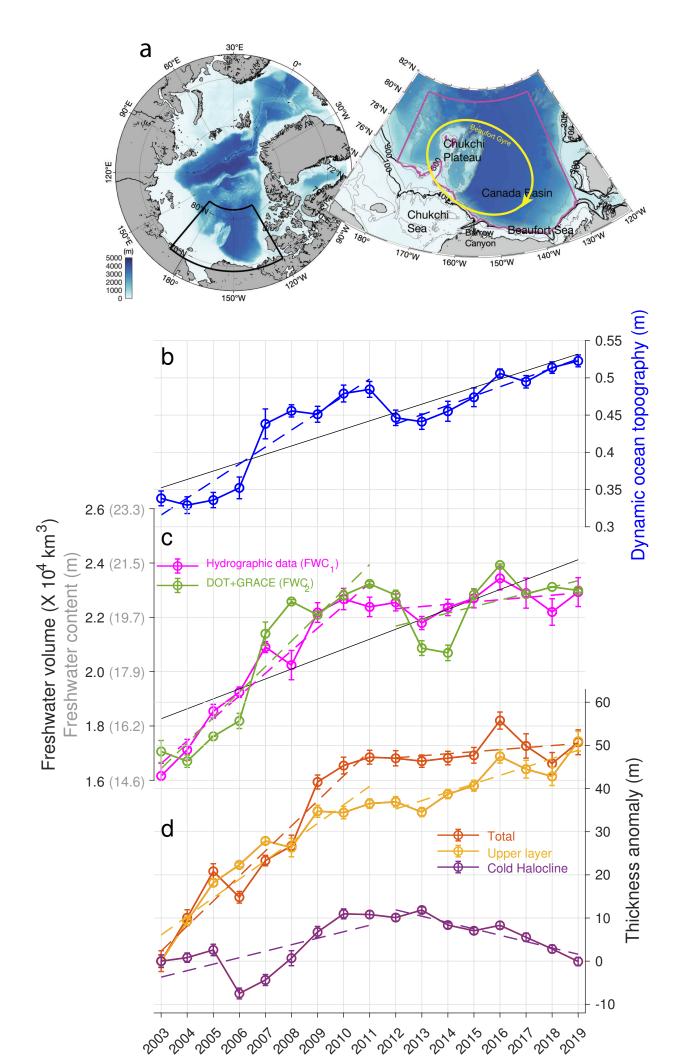
- 544 (5) Pacific Marine Environmental Laboratory (PMEL, https://www.pmel.noaa.gov/epic/ewb/);
- 545 (6) NOAA Alaska Fisheries Science Center (https://data.eol.ucar.edu/dataset/);
- 546 (7) University of Alaska Fairbanks Institute of Marine Science (UAFIMS, available at the Arctic
- 547 Ocean Observing System, http://www.aoos.org);
- 548 (8) Fisheries and Oceans Canada's Institute of Ocean Sciences (IOS,
- 549 https://www.pac.dfompo.gc.ca/science/index-eng. html);
- 550 (9) Japan Agency for Marine-Earth Science and Technology (JAMSTEC,
- 551 http://www.godac.jamstec. go.jp/darwin/e/).
- 552 (10) Korea Polar Data Center (https://kpdcopen.kopri.re.kr)
- 553 The dynamic ocean topography data produced by Armitage et al. (2016) can be found at
- 554 http://www.cpom.ucl.ac.uk/dynamic\_topography, and the updated dynamic ocean topography
- data from 2011-2019 is available at http://www.cpom.ucl.ac.uk/dynamic\_topography/. The
- 556 GRACE data can be accessed via https://sealevel.nasa.gov/data/dataset/?identifier=SLCP\_CSR-
- 557 RL06-Mascons-v02\_RL06\_v02. The ERA5 reanalysis data can be obtained from the European
- 558 Center for Medium-Range Weather Forecasts
- 559 (https://rmets.onlinelibrary.wiley.com/doi/10.1002/qj.3803). The GLORYS12 reanalysis is
- 560 available at the Copernicus Marine and Environment Monitoring Service
- 561 (http://www.marine.copernicus.eu). The JAMSTEC mooring data at the mouth of the Barrow
- 562 Canyon from 2003-2019 are available at https://www.jamstec.go.jp/iace/e/report/. The
- 563 monthly timeseries of Arctic Oscillation index is obtained from NOAA's Climate Prediction
- 564 Center (https://www.cpc.ncep.noaa.gov/products/precip/CWlink/daily\_ao\_index/ao.shtml).
- 565 The bathymetry data used in the study are from the International Bathymetric Chart of the
- 566 Arctic Ocean (IBCAO) version 3 49
- 567 (https://www.gebco.net/about\_us/committees\_and\_groups/scrum/ibcao/ibcao\_v3.html).
- 568

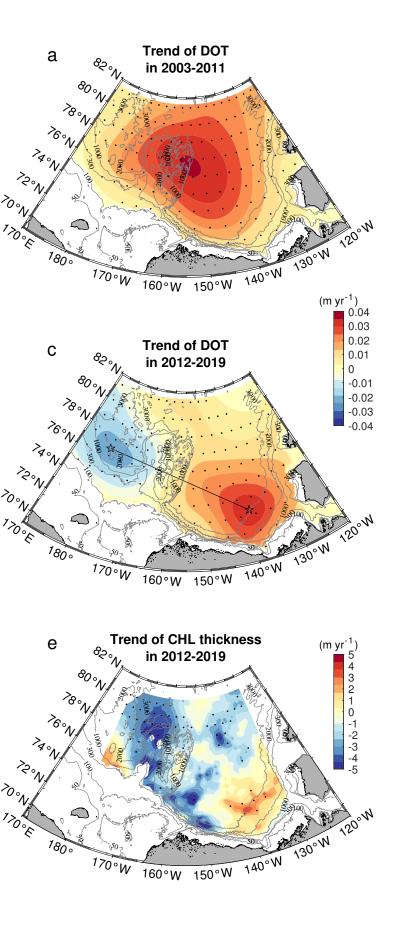
# 569 Code availability

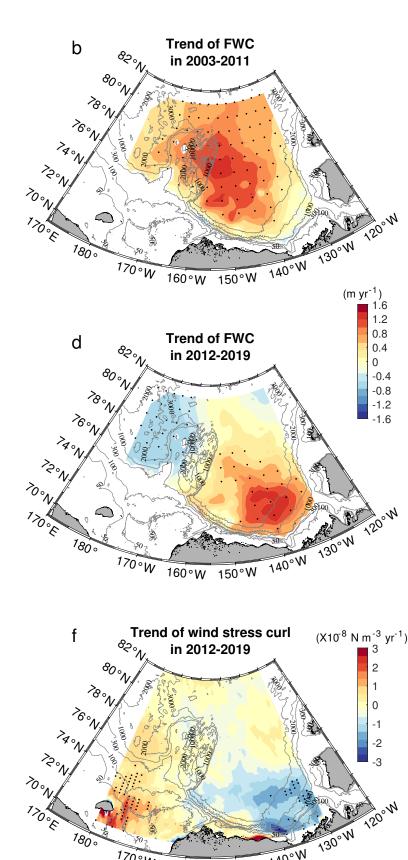
- 570 The Matlab scripts used to compute the freshwater content and to calculate the Lagrangian
- 571 particle trajectories can be accessed upon request to P.L.
- 572

## 573 Methods-only references

- 57439Behrendt, A., Sumata, H., Rabe, B. & Schauer, U. UDASH–Unified Database for Arctic and575Subarctic Hydrography. *Earth System Science Data* **10**, 1119-1138 (2018).
- 576 40 Danielson, S. *et al.* Manifestation and consequences of warming and altered heat fluxes
  577 over the Bering and Chukchi Sea continental shelves. *Deep Sea Res. II* **177**, 104781
  578 (2020).
- 579 41 Smith, W. & Wessel, P. Gridding with continuous curvature splines in tension.
  580 *Geophysics* 55, 293-305 (1990).
- 58142Armitage, T. W. *et al.* Arctic sea surface height variability and change from satellite radar582altimetry and GRACE, 2003–2014. *J. Geophys. Res. Oceans* **121**, 4303-4322 (2016).
- 43 Hersbach, H. Operational global reanalysis: progress, future directions and synergies
  584 with NWP. (European Centre for Medium Range Weather Forecasts, 2018).
- 58544Lellouche, J.-M. *et al.* The Copernicus global 1/12° oceanic and sea ice GLORYS12586reanalysis. Frontiers in Earth Science **9**, 585 (2021).
- 587 45 Woodgate, R. A. Increases in the Pacific inflow to the Arctic from 1990 to 2015, and 588 insights into seasonal trends and driving mechanisms from year-round Bering Strait 589 mooring data. *Prog. Oceanogr.* **160**, 124-154 (2018).
- 590 46 Save, H., Sun, A. Y., Scanlon, B. R. & Rateb, A. in *AGU Fall Meeting Abstracts.* G001-001.
- 591 47 Marshall, J. & Radko, T. Residual-mean solutions for the Antarctic Circumpolar Current 592 and its associated overturning circulation. *J. Phys. Oceanogr.* **33**, 2341-2354 (2003).
- 59348Bourgain, P. & Gascard, J.-C. The Arctic Ocean halocline and its interannual variability594from 1997 to 2008. Deep Sea Res. I 58, 745-756 (2011).
- 59549Jakobsson, M. *et al.* The international bathymetric chart of the Arctic Ocean (IBCAO)596version 3.0. *Geophys. Res. Lett.* **39** (2012).
- 597
- 598
- 599
- 600
- ....
- 601
- 602







140°W

160°W 150°W

1800

170°W

